inorganics

MDPI

Article

In Situ Mullite Formation in 80 wt% Alumina Ceramics via Kaolin/$Ca_3(PO_4)_2$ Ratio Modulation: Densification, Microstructural Evolution, and Dielectric Breakdown Behavior

Shaomin Lin [1,†], Yaling Yu [1,†], Xin Chen [1], Haiyin Huang [2], Leilei Cai [2], Wei Xu [3,*] and Chenyang Zhang [1,3,*]

[1] Advanced Ceramics Innovation & Research Center, Hanshan Normal University, Chaozhou 521041, China
[2] School of Materials Science and Engineering, Hanshan Normal University, Chaozhou 521041, China
[3] School of Materials Science and Engineering, South China University of Technology, Guangzhou 510640, China
* Correspondence: weixu_my@163.com (W.X.); zhangchenyang@hstc.edu.cn (C.Z.)
† These authors contributed equally to this work.

Abstract

Mullite–alumina composite ceramics were fabricated via in situ reaction sintering by modulating the kaolin-to-calcium phosphate (K/C) mass ratio (3, 6, 9, and 12) within an 80 wt% alumina matrix. The effects of liquid-phase sintering aid content on densification, phase evolution, microstructural development, and dielectric breakdown reliability were systematically investigated. X-ray diffraction confirmed corundum and mullite as the predominant phases across all compositions, with the mullite yield exhibiting a non-monotonic dependence on the K/C ratio. The optimal K/C ratio of 9 yielded the highest mullite content (9.15 wt%), the greatest bulk density (3.58 g·cm^{-3}), and an apparent porosity (4.3%), attributable to a balanced liquid-phase volume and viscosity that promoted dissolution–precipitation transport while suppressing gas entrapment. Quantitative microstructural analysis revealed an average alumina grain size of 5.17 μm and uniform distribution of acicular mullite grains within the corundum matrix. Weibull statistical analysis of the dielectric breakdown strength for the optimal composition (K/C = 9) gave a characteristic breakdown strength E_0 of 14.31 kV/mm and a Weibull modulus m > 20, indicating exceptional data reliability. The high breakdown resistance is ascribed to the synergistic effects of reduced porosity, increased grain boundary density, and residual compressive stresses at mullite–corundum interfaces. These findings establish a quantitative correlation among liquid-phase content, microstructural optimization, and dielectric reliability, providing a framework for the compositional design of cost-effective alumina-based energy storage ceramics.

Keywords: alumina ceramic; mullite; in-situ synthesis; dielectric breakdown strength; Weibull distribution

Check for updates

Academic Editor: Christian Julien

Received: 22 August 2026
Revised: 9 October 2026
Accepted: 13 October 2026
Published: 15 October 2026

Copyright: © 2026 by the authors. Licensee MDPI, Basel, Switzerland. This article is an open access article distributed under the terms and conditions of the Creative Commons Attribution (CC BY) license.

1. Introduction

The global energy transition, together with the rapid development of pulsed power systems, renewable energy grid integration, and electric vehicle technologies, has driven a sustained surge in demand for high-reliability dielectric energy storage materials [1,2]. Alumina (Al_2O_3) ceramics have found longstanding industrial applications in high-voltage insulators and power module packaging, owing to the abundant raw material availability, low cost, moderate dielectric constant ($\varepsilon_r \approx 9$–10), and intrinsically high dielectric breakdown strength (15–22 kV/mm) [3–5]. Nevertheless, conventional high-purity alumina

ceramics typically require sintering temperatures as high as 1600–1700 °C [2,6]. Moreover, the performance enhancement of single-phase alumina has approached its intrinsic limit, restricting its broader deployment in energy storage devices operating under demanding conditions [7,8].

To circumvent these limitations, alumina-based multiphase ceramic systems have attracted considerable attention. Among them, the incorporation of mullite ($3Al_2O_3 \cdot 2SiO_2$) as a secondary phase has emerged as an effective approach to improving the multifunctional properties of alumina ceramics. The introduction of mullite whiskers or grains can toughen the brittle alumina matrix through crack deflection, whisker pull-out, and grain boundary strengthening mechanisms, yielding substantial improvements in mechanical and thermal properties while maintaining satisfactory insulating performance [9–12]. Consequently, mullite–alumina composite ceramics, which integrate structural and functional attributes, demonstrate considerable promise for dielectric energy storage applications [13].

For linear dielectric materials, the recoverable energy storage density is governed by the equation $J = \frac{1}{2}\varepsilon_0\varepsilon_r E_b^2$, where Eb denotes the dielectric breakdown strength. Since the energy density scales quadratically with the breakdown field, even a marginal improvement in dielectric breakdown strength can lead to a substantial gain in energy density [14–17]. Therefore, dielectric breakdown strength serves as a critical metric for evaluating the performance of energy storage ceramics and directly dictates the upper limit of energy density in capacitor devices. Although the mechanical and thermal properties of mullite–corundum composite ceramics have been extensively investigated [18,19], a quantitative understanding of the dielectric breakdown behavior of alumina-based composites containing in-situ synthesized mullite is still lacking [20]. This knowledge gap significantly constrains the rational design of such materials for energy storage applications.

Mullite is conventionally synthesized from kaolin ($Al_2O_3 \cdot 2SiO_2 \cdot 2H_2O$) via decomposition and solid-state reactions at approximately 1200–1400 °C [21]. The addition of sintering aids can effectively lower the mullite formation temperature and modulate its morphology and distribution. Calcium phosphate ($Ca_3(PO_4)_2$), a typical liquid-phase sintering aid, decomposes at elevated temperatures to generate CaO and P_2O_5, forming low-eutectic liquid phases that facilitate ionic diffusion and mass transport. Previous studies have demonstrated that the incorporation of calcium phosphate into kaolin can induce the formation of high-aspect-ratio mullite whiskers at relatively low temperatures, and the aspect ratio and yield of mullite can be precisely controlled by adjusting the calcium phosphate content [22,23]. Building upon these findings, the present study employs an 80 wt% alumina matrix and systematically modulates the kaolin-to-calcium phosphate mass ratios (3, 6, 9, and 12) to design a gradient of liquid-phase sintering aids. The work aims to address the following scientific questions: (1) the non-monotonic regulation of liquid-phase content on densification behavior (bulk density, shrinkage, and porosity); (2) the in situ yield, morphological evolution, and distribution characteristics of mullite under varying liquid-phase environments; and (3) the power-frequency dielectric breakdown strength and Weibull statistical reliability of the optimal composition. By establishing a quantitative correlation among liquid-phase sintering aid content, densification, microstructure, and dielectric breakdown reliability, this study provides experimental evidence and theoretical guidance for the compositional design and performance optimization of cost-effective alumina-based energy storage ceramics.

2. Results and Discussion

2.1. Phase Composition and Evolution

Figure 1 presents the XRD patterns of the sintered samples with varying kaolin-to-calcium phosphate (K/C) mass ratios. All samples exhibited α-Al_2O_3 (corundum, PDF

No. 76-0144) and $3Al_2O_3 \cdot 2SiO_2$ (mullite, PDF No. 15-0776) as the predominant crystalline phases, confirming the successful in-situ formation of mullite within the alumina matrix. For the sample with the lowest K/C ratio of 3 (KC1), weak diffraction peaks attributable to secondary phases were detected, which are ascribed to the reaction of excess CaO (derived from $Ca_3(PO_4)_2$ decomposition) with Al_2O_3 and SiO_2 at elevated temperatures. As the K/C ratio increased, these secondary phases gradually diminished, indicating that an appropriate calcium phosphate content suppresses the formation of undesirable impurity phases.

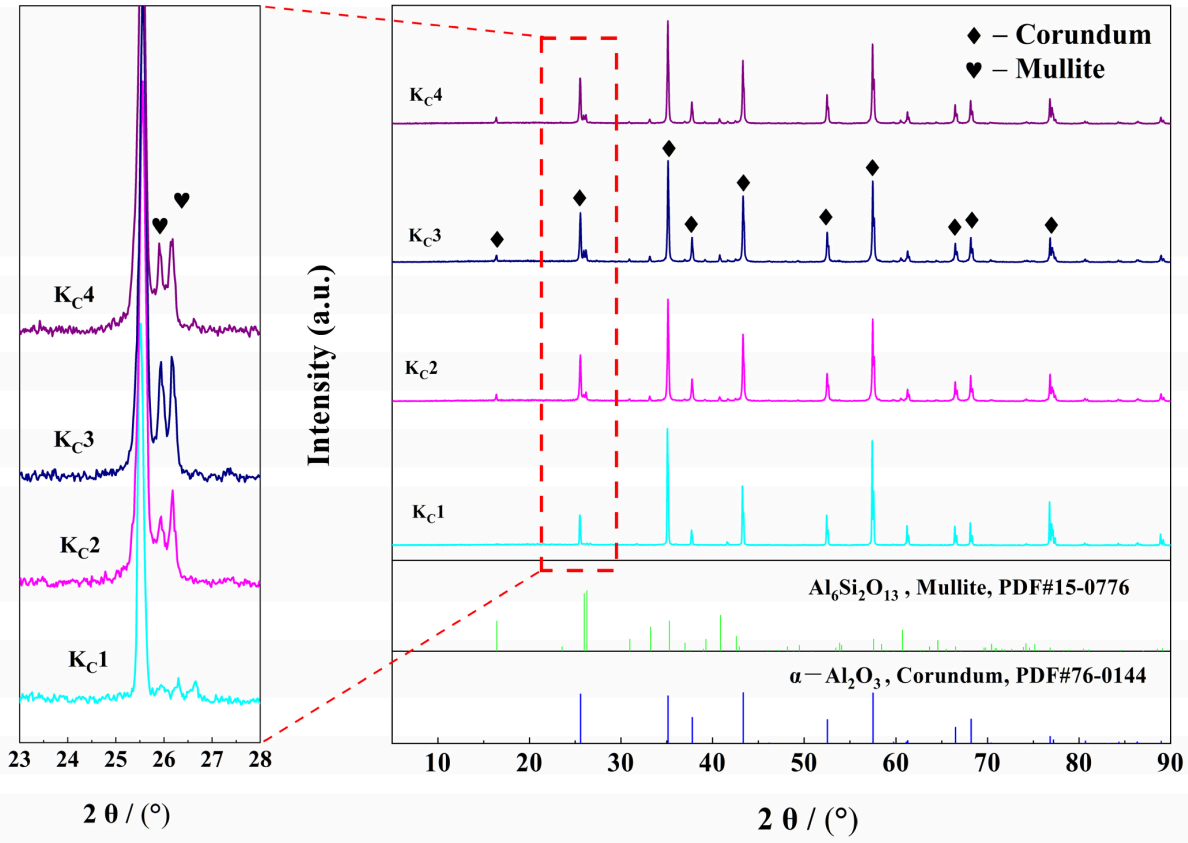


Figure 1. The XRD spectra of the sintered samples.

Semi-quantitative phase analysis (Table 1) revealed a non-monotonic variation in mullite content with increasing K/C ratio. The mullite fraction increased from 5.03 wt% (K/C = 3) to 9.15 wt% (K/C = 9), accompanied by a decrease in the relative intensity of corundum reflections. However, upon further increasing the K/C ratio to 12, the mullite content slightly decreased to 8.89 wt%, while the "Others" fraction (encompassing amorphous and minor crystalline phases) continued to decline from 18.85 wt% (K/C = 3) to 12.14 wt% (K/C = 12).

Table 1. Phase quantification (wt%) of sintered samples by XRD semi-quantitative analysis.

Sample	Corundum	Mullite	Others	K/C Ratio
K_C1	76.12	5.03	18.85	3
K_C2	78.24	7.29	14.47	6
K_C3	78.52	9.15	12.33	9
K_C4	78.97	8.89	12.14	12

This trend can be rationalized by the competing roles of liquid-phase content in mullite crystallization. At K/C = 3, the relatively high $Ca_3(PO_4)_2$ content (5.00 wt% of

the total batch) generates an excessive amount of low-viscosity liquid phase at elevated temperatures. While this facilitates ionic mobility, the excess CaO concurrently reacts with the aluminosilicate species to form calcium-rich secondary phases rather than stoichiometric mullite, thereby suppressing the mullite yield. At K/C = 9, the liquid-phase volume and viscosity are optimally balanced, providing favorable mass transport channels for mullite nucleation and growth while minimizing parasitic reactions. Conversely, at K/C = 12, the reduced $Ca_3(PO_4)_2$ content (1.54 wt%) produces insufficient liquid phase, diminishing the ionic diffusion rate and limiting the extent of mullitization. The progressive reduction in the "Others" fraction with increasing K/C ratio further corroborates the diminishing liquid-phase residue and the enhanced degree of mullite crystallization.

2.2. Densification Behavior

The densification parameters of the sintered samples are summarized in Table 2. All metrics—including bulk density and linear shrinkage—exhibited a distinct non-monotonic dependence on the K/C ratio, reaching an optimum at K/C = 9 (sample K_C3). Specifically, K_C3 achieved the highest bulk density (3.58 $g \cdot cm^{-3}$) and the greatest shrinkage, indicative of optimal densification.

Table 2. Physical properties and densification parameters of sintered samples.

Sample	Bulk Density ($g \cdot cm^{-3}$)	Water Absorption (%)	Linear Shrinkage (%)
K_C1	3.51	0.24	11.18
K_C2	3.55	0.35	11.46
K_C3	3.58	0.39	12.15
K_C4	3.57	0.43	11.87

This non-monotonic behavior can be interpreted through the framework of liquid-phase sintering theory. At low K/C ratios (e.g., K/C = 3), the elevated $Ca_3(PO_4)_2$ content (5 wt% relative to the total batch) generates an excessive volume of low-viscosity liquid phase. Although this promotes rapid particle rearrangement during the initial sintering stage, the surplus liquid becomes susceptible to gas entrapment, forming bubbles in the later stage. Moreover, the excessive fluidity at high temperatures can induce specimen distortion; both phenomena are detrimental to final densification. At the opposite extreme (K/C = 12), the $Ca_3(PO_4)_2$ content is insufficient (1.54 wt%), yielding inadequate liquid phase to effectively fill interparticle voids or drive dissolution–precipitation mass transport. Consequently, the sintering driving force is markedly reduced, leading to inferior densification. Only at the intermediate K/C ratio of 9 does the liquid-phase content and viscosity achieve an optimal balance: sufficient to promote particle rearrangement and dissolution–precipitation transport, yet insufficient to cause bubble entrapment or dimensional distortion, thereby yielding the highest degree of densification.

2.3. Microstructural Evolution

Figure 2 presents the ultra-high-magnification optical micrographs of the sintered samples across the K/C ratio gradient. At K/C = 3 (Figure 2a), the microstructure is characterized by a substantial glassy phase content, which obscures grain boundaries and rounds the crystal edges of both corundum and mullite grains. The in-situ-formed mullite appears as elongated grains or whiskers uniformly dispersed within the corundum matrix. As the K/C ratio increases, the glassy phase content progressively decreases, and grain boundaries become increasingly discernible. At K/C = 9 (Figure 2c), the sample exhibits the largest grain size with a relatively uniform distribution; occasional submicron pores are visible, yet the overall microstructural homogeneity is superior. At K/C = 12 (Figure 2d),

the average grain size decreases relative to K_C3, indicating that insufficient liquid phase has restricted alumina grain growth. Concurrently, the microporosity increases, consistent with the reduced densification efficiency observed in Section 3.2.

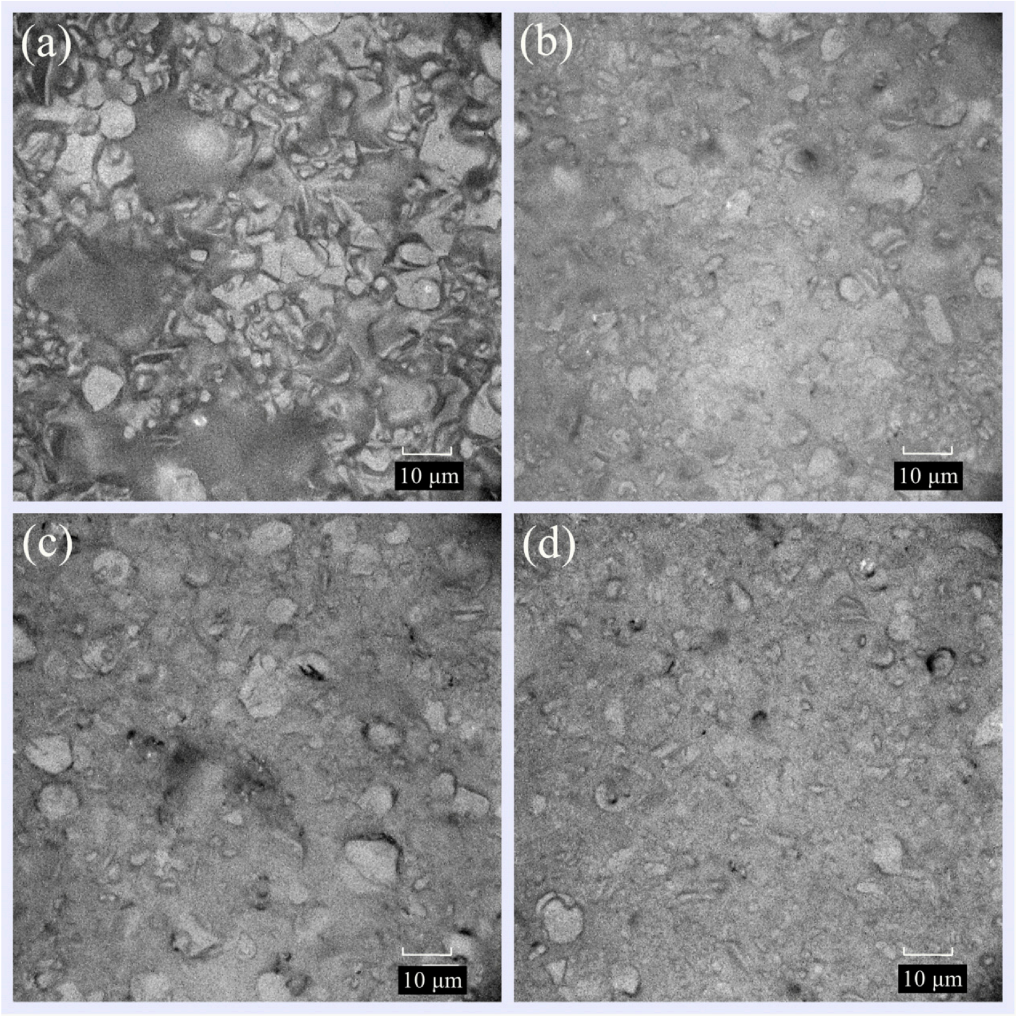


Figure 2. Ultra-high-magnification optical micrographs of samples with varying kaolin/$Ca_3(PO_4)_2$ mass ratios. ((**a**), K_C1, K/C = 3; (**b**), K_C2, K/C = 6; (**c**),K_C3, K/C = 9; (**d**), K_C4, K/C = 12).

To elucidate the structure–property relationship of the optimally densified composition, detailed microstructural characterization was performed on sample K_C3 (K/C = 9). The EDS maps and SEM/BSE images have been presented in Figures 3 and 4. The corundum (α-Al_2O_3) grains are characterized by strong Al Kα signals (Figure 3b,d,f), whereas the mullite ($3Al_2O_3 \cdot 2SiO_2$) grains and glassy phase exhibit concurrent Al and Si enrichment around the corundum grains (Figures 3b–d,g and 4a). Figure 4a shows the SEM micrograph of an HF-etched surface, revealing an interlocking microstructure comprising equiaxed corundum grains and acicular/whisker-like mullite grains. Ca is concentrated exclusively at grain boundaries and triple junctions, co-localizing with Si enrichment in the intergranular regions. This elemental partitioning confirms that Ca remains predominantly in the residual glassy phase, having served its fluxing role during sintering and contributing to the formation of mullite whiskers. The three glass-network-forming/modifying elements—Al (from kaolin or corundum), Si (from kaolin), Ca/P (from $Ca_3(PO_4)_2$)—react at elevated temperatures to form low-melting eutectic liquid phases, forming an amorphous intergranular glassy phase at the cooling stage. This distinct contrast in elemental composition allows

the two phases to be unambiguously distinguished by energy-dispersive spectroscopy, corroborating the phase identification obtained from XRD.

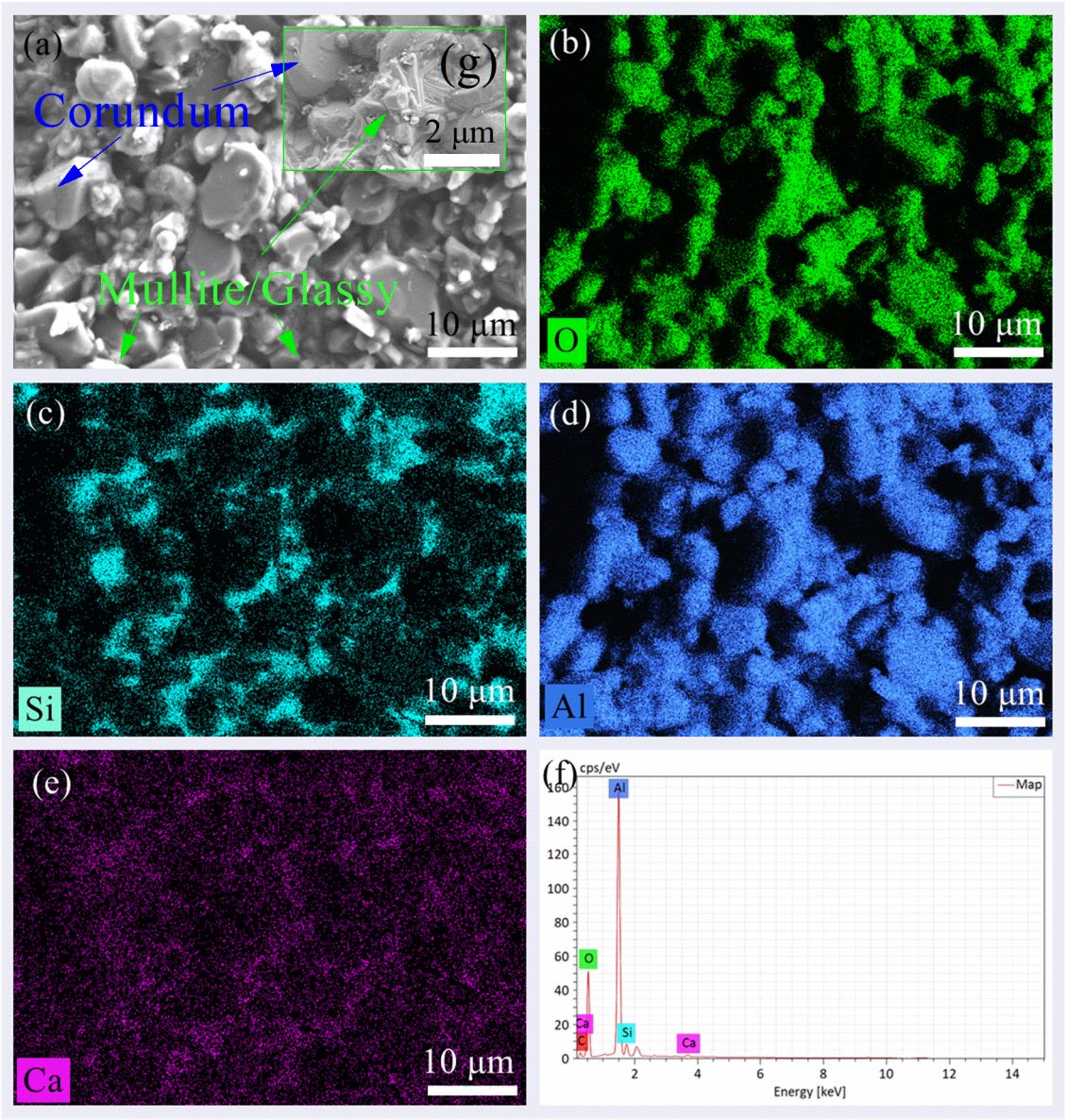


Figure 3. Microstructural and elemental characterization of the KC3 sample: (**a**) SEM micrograph; (**b**–**e**) EDS elemental distribution maps of (**b**) O, (**c**) Si, (**d**) Al, and (**e**) Ca; (**f**) corresponding EDS spectrum; (**g**) high-magnification SEM micrograph.

The corresponding BSE image (Figure 4b) provides atomic-number contrast: the brighter regions correspond to corundum (higher average atomic number), while the darker regions represent mullite (lower average atomic number), confirming the uniform spatial distribution of the secondary phase. Quantitative image analysis yielded an average grain size of 5.17 μm and a porosity of 4.3%. The porosity value is consistent with the physical property measurements in Section 3.2, corroborating satisfactory overall densification, albeit with residual scope for optimization. The residual pores are primarily attributed to gas entrapment during liquid-phase sintering and incomplete liquid expulsion accompanying rapid grain growth.

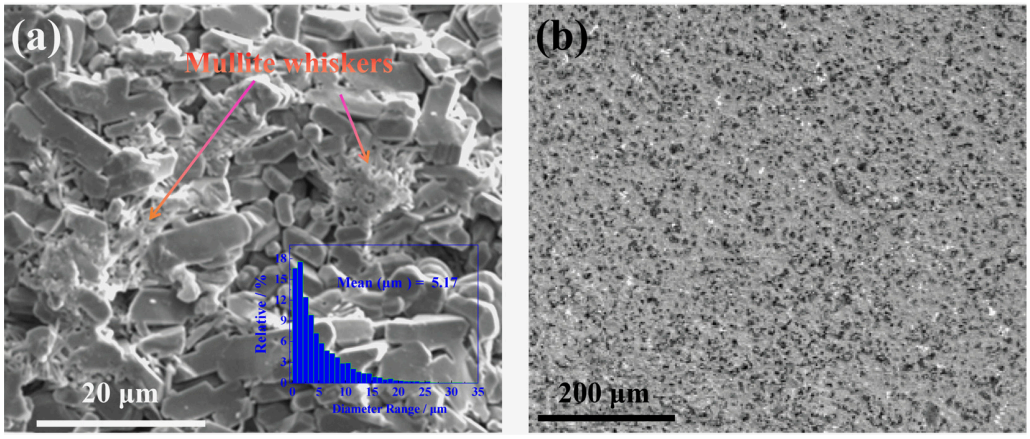


Figure 4. Microstructural characterization of the KC3 sample: (**a**) scanning electron micrograph (SEM) and (**b**) backscattered electron (BSE) image.

2.4. Dielectric Breakdown Behavior

The dielectric breakdown characteristics were systematically evaluated for the optimally densified composition (K_C3, K/C = 9) to establish a quantitative link between microstructure and dielectric reliability.

The breakdown strength data were analyzed using the two-parameter Weibull distribution (Equation (1)). Figure 5 presents the Weibull probability plot, where the linearity of the data confirms the applicability of the Weibull model. Least-squares regression yielded a characteristic breakdown strength E_0 of 14.31 kV/mm (for a specimen thickness of 1.80 mm) and a Weibull modulus m > 20, with a coefficient of determination R^2 close to unity. The exceptionally high Weibull modulus indicates minimal data scatter and high statistical reliability of the measured breakdown strength.

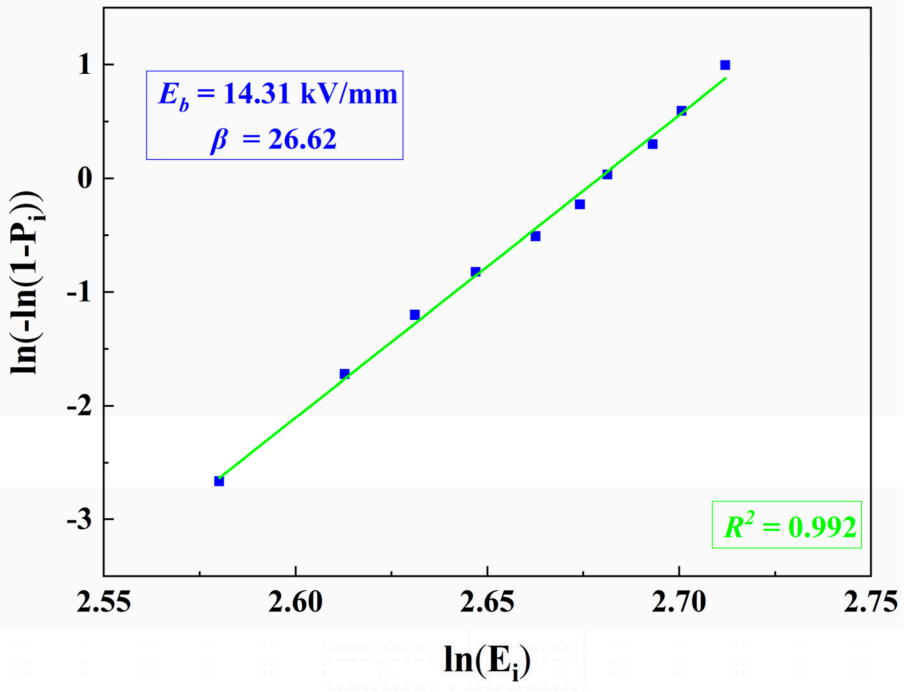


Figure 5. Weibull two-parameter distribution of dielectric breakdown strength (DBS) for mullite-alumina ceramics (K_C3).

The high dielectric reliability of the K_C3 composition originates from the synergistic interplay of three microstructural factors:

Densification effect: The moderate liquid-phase content at K/C = 9 promotes uniform densification, minimizing the population and size of pores—which serve as critical defects initiating electrical breakdown. The low porosity of 4.3% reduces the probability of pore-induced field concentration.

Grain boundary engineering: The uniformly distributed in situ-formed mullite grains refine the corundum matrix and increase the grain boundary density. A higher density of grain boundaries impedes the propagation of breakdown paths by forcing frequent deflection, and promotes a more homogeneous electric field distribution throughout the ceramic volume.

Residual compressive stress: The moderate thermal expansion mismatch between mullite (~4.5×10^{-6} K^{-1}) and corundum (~8.0×10^{-6} K^{-1}) introduces localized compressive stresses at grain boundaries upon cooling from the sintering temperature. These compressive stresses suppress the nucleation and propagation of microcracks under electrical loading, which may enhance the intrinsic breakdown resistance.

The characteristic breakdown strength of 14.31 kV/mm, while lower than the intrinsic value of high-purity alumina (15–22 kV/mm), is competitive for medium-to-low voltage energy storage applications, particularly given the substantially reduced processing cost and sintering temperature afforded by the liquid-phase sintering strategy. Furthermore, the theoretical energy storage density of the 80 wt% alumina–mullite composite can be estimated using the linear dielectric equation. Adopting an effective dielectric constant $\varepsilon_r \approx 9.5$ for the mullite–corundum composite, the recoverable energy density is approximately ~8.6×10^{-3} $J \cdot cm^{-3}$. This value, combined with the high Weibull reliability ($m > 20$), demonstrates the potential of in-situ-formed mullite-reinforced alumina ceramics for cost-effective energy storage and capacitor applications. Further enhancement in breakdown strength is anticipated through refined sintering protocols aimed at reducing the residual porosity below the current 4.3% level.

3. Materials and Methods

3.1. Raw Materials and Formulation Design

α-Al_2O_3 powder (≥99.0% purity, average particle size ~2–6 μm) was employed as the matrix material. Kaolin (main constituent: kaolinite, $Al_2O_3 \cdot 2SiO_2 \cdot 2H_2O$, ≥95% purity) served as the aluminosilicate precursor for in-situ mullite formation, and calcium phosphate ($Ca_3(PO_4)_2$, analytical reagent grade) was used as the liquid-phase sintering aid. Based on preliminary experiments, the alumina content was fixed at 80 wt%, and four batch formulations with varying kaolin-to-calcium phosphate mass ratios (denoted as K/C = 3, 6, 9, and 12) were designed by adjusting the relative proportions of kaolin and $Ca_3(PO_4)_2$. An alumina content of 80 wt% was selected as a baseline based on preliminary experiments. Calcium phosphate preferentially promotes mullite whisker formation from the aluminosilicate precursor without reacting extensively.

The chemical composition of the kaolin raw material is presented in Table 3, and its phase purity is confirmed by the XRD pattern shown in Figure 6; the detailed batch formulations are summarized in Table 4. This gradient design was intended to systematically investigate the influence of liquid-phase content on the yield and morphology of in-situ mullite and the densification behavior of the resulting composite ceramics.

Table 3. Chemical composition of kaolin (wt%).

Sample	SiO_2	Al_2O_3	Fe_2O_3	K_2O	Others	LOI
Kaolin	50.87	37.96	0.57	0.37	0.02	10.21

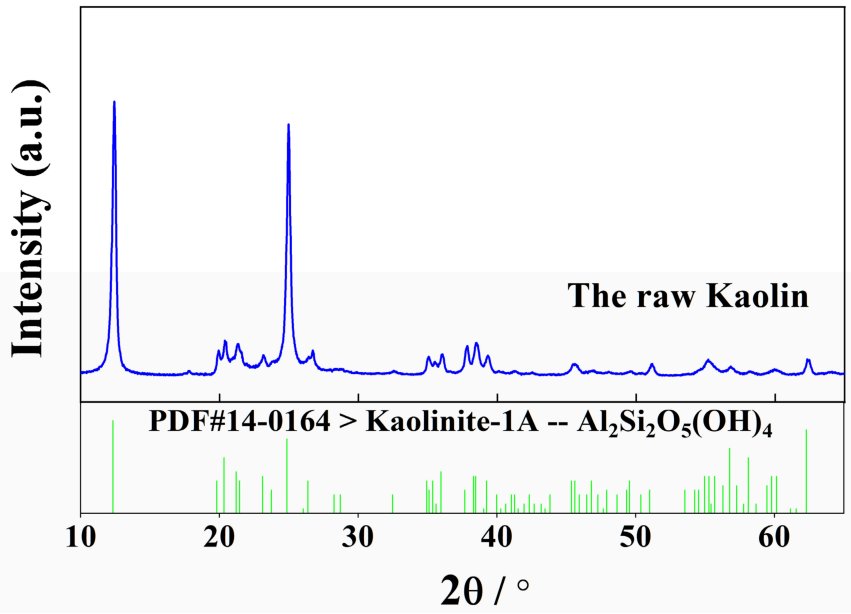


Figure 6. The XRD spectrum of the kaolin.

Table 4. Batch formulations of samples with varying kaolin/$Ca_3(PO_4)_2$ mass ratios.

Sample	Al_2O_3 (wt%)	Kaolin (wt%)	$Ca_3(PO_4)_2$ (wt%)	Kaolin/$Ca_3(PO_4)_2$
K_C1	80	15	5	3
K_C2	80	17.14	2.86	6
K_C3	80	18.00	2.00	9
K_C4	80	18.46	1.54	12

3.2. Sample Preparation

The raw materials were accurately weighed according to the formulations given in Table 4 and placed in a polyurethane ball-milling jar. Deionized water and alumina milling media (ball-to-powder mass ratio of 2:1) were added, and the mixture was ball-milled at 400 rpm for 6 h to achieve homogeneous mixing and particle size reduction. After milling, the alumina balls were separated using a sieve. Subsequently, 1 wt% polyvinyl alcohol (PVA, degree of polymerization 1750 ± 50) was added to the slurry as a binder. After thorough stirring and dispersion, the slurry was granulated by spray drying (Inlet temperature, 200 °C; slurry feed rate, 800 mL·h^{-1}; and anti-blocking needle actuation interval, 3 s.) to obtain spherical powders with good flowability. The dried powders were uniaxially pressed into disk-shaped green compacts (30 mm in diameter) in a stainless steel mold at 200 MPa. The green bodies were then sintered at 1580 °C for 80 min according to the thermal schedule shown in Figure 7 (heating rate, dwell temperature, and duration as indicated), followed by furnace cooling to room temperature. The thickness of the sintered samples was controlled at 1.80 ± 0.05 mm by grinding for subsequent dielectric breakdown testing.

3.3. Characterization and Testing

The phase composition of the sintered samples was analyzed by X-ray diffraction (XRD, MiniFlex 600, Rigaku, Tokyo, Japan) using Cu Kα radiation in the 2θ range of 5–90°. Semi-quantitative phase analysis was performed using PDXL 2.0 software (Rigaku, Tokyo, Japan) via the external standard method with high-purity Si as the external reference.

The microstructure of the fracture surface was examined by microscopy (Ultra-high-magnification optical microscopy, KH-8700, HIROX, Hirox Co., Ltd. Inc., Tokyo, Japan; scan-

ning electron microscopy, SEM, Nova NanoSEM 430, Thermo Fisher Scientific, Waltham, MA, USA). For SEM observation, the samples were etched with hydrofluoric acid (HF), ultrasonically cleaned, and sputter-coated with platinum. The bulk density and water absorption of the sintered samples were measured by the Archimedes method using deionized water as the immersion medium. Linear shrinkage was calculated from dimensional measurements of the green and sintered bodies.

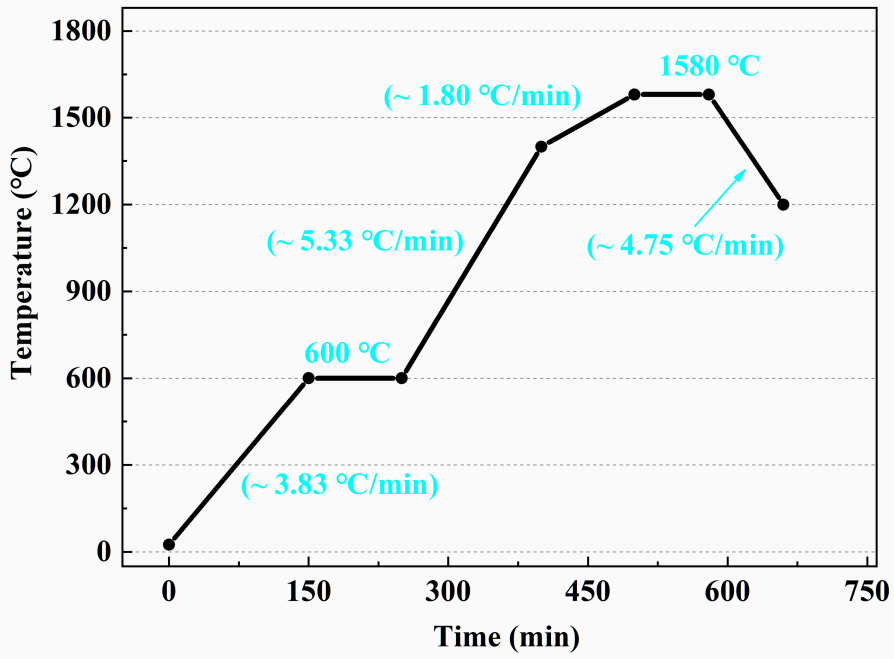


Figure 7. The sintering curves of the green bodies.

Grain size was determined by the linear intercept method (ISO 13383-1:2012) [24]. Porosity was quantified via binary image processing of backscattered electron (BSE) micrographs using ImageJ software (version 1.54, National Institutes of Health, Bethesda, MD, USA).

Dielectric breakdown strength testing was performed using a 1.8 mm diameter sphere–sphere electrode system in No. 25 transformer oil, with voltage ramped at 1.0 kV/s under AC conditions at 50 Hz until breakdown (IBVAD-50, Guilin Saimei Testing Technology Co., Ltd., Guilin, China). At least 10 specimens were tested per group. The breakdown voltage (kV) was recorded for each specimen and divided by its measured thickness (mm) to obtain the dielectric breakdown strength (DBS, kV/mm). The DBS data were statistically processed using the Weibull distribution:

$$P(E) = 1 - \exp\left[-\left(\frac{E}{E_0}\right)^m\right] \quad (1)$$

where E is the measured breakdown strength, E0 is the characteristic breakdown strength, and m is the Weibull modulus, which characterizes data dispersion and material reliability. Linearization via double logarithmic transformation yields the following:

$$\ln[-\ln(1 - P(E))] = m\ln(E) - m\ln(E_0) \quad (2)$$

4. Conclusions

This study demonstrates that the kaolin-to-calcium phosphate ratio serves as a critical control parameter for controlling the in-situ formation of mullite and the densification behavior of 80 wt% alumina ceramics. The mullite content exhibited a non-monotonic

dependence on the K/C ratio, peaking at 9.15 wt% when K/C = 9. At low K/C ratios (e.g., K/C = 3), excessive calcium phosphate promoted the formation of calcium aluminosilicate impurity phases, whereas at high K/C ratios (e.g., K/C = 12), insufficient liquid phase limited the extent of mullitization. Consequently, bulk density and linear shrinkage reached extrema at K/C = 9, whereas the water absorption exhibited a more complex dependence on the liquid-phase content. The liquid-phase content (2.00 wt% $Ca_3(PO_4)_2$) achieved an optimal balance between particle rearrangement and dissolution–precipitation transport without inducing bubble entrapment or specimen distortion. This yielded a maximum bulk density of 3.58 $g \cdot cm^{-3}$ and a porosity of 4.3%.

The optimally densified composition (K_C3) exhibited an interlocking microstructure comprising equiaxed corundum grains with an average size of 5.17 μm and uniformly distributed acicular mullite grains, the spatial uniformity of which was further corroborated by backscattered electron imaging. This refined microstructure translated directly into superior dielectric reliability: the K_C3 sample achieved a characteristic AC breakdown strength of 14.31 kV/mm with a Weibull modulus m > 20, signifying minimal data scatter and high statistical reproducibility. The enhanced breakdown resistance originates from the synergistic interplay of three factors—reduced porosity, increased grain boundary density, and thermally induced compressive stresses at mullite–corundum interfaces—which collectively impede the propagation of breakdown paths.

Given the high breakdown reliability and the estimated recoverable energy density, the in-situ-formed mullite-reinforced alumina composite is a promising candidate for medium-to-low voltage energy storage applications.

Author Contributions: Software, X.C.; formal analysis, X.C., H.H. and Y.Y.; investigation, X.C., H.H., W.X. and L.C.; data curation, C.Z., H.H. and L.C.; writing—original draft preparation, S.L. and Y.Y.; writing—review and editing, W.X. and C.Z.; supervision, W.X. and C.Z.; funding acquisition, S.L. and X.C. All authors have read and agreed to the published version of the manuscript.

Funding: The Special Project in Key Fields of General Universities in Guangdong Province (2024ZDZX3030 and 2024ZDZX3029), the Mentorship Support Program of Hanshan Normal University (XWT2025101).

Institutional Review Board Statement: Not applicable.

Informed Consent Statement: Not applicable.

Data Availability Statement: The original contributions presented in this study are included in the article. Further inquiries can be directed to the corresponding authors.

Acknowledgments: The Advanced Ceramic Materials Innovation Research Center is acknowledged. The Guangdong Chaoshan Institute of Higher Education and Technology is acknowledged.

Conflicts of Interest: The authors declare no conflict of interest.

References

1. Ning, Y.; Pu, Y.; Wu, C.; Zhang, J.; Zhang, X.; Shang, Y. Achieving high energy storage performance below 200 kV/cm in $BaTiO_3$-based medium-entropy ceramics. *Ceram. Int.* **2023**, *49*, 20326–20333. [CrossRef]
2. Xu, L.-Y.; Ouyang, J.; Cheng, Z.-X.; Huan, Y. A review on the dielectric ceramics for high energy-storage application. *Adv. Ceram.* **2025**, *46*, 195–246. [CrossRef]
3. Naga, S.M.; El-Mehalawy, N.; Awaad, M.; Eliyan, T. Dielectric properties of nano-(MgO-Gd_2O_3) co-doped alumina for high voltage insulators. *Ceram. Int.* **2020**, *46*, 28390–28399. [CrossRef]
4. Du, J.; Yi, X.; Li, M.; Peng, K. Fabricating a denser SiO_2–CaO co-doped 95 wt% alumina ceramic to verify that small pores have no effect on the dielectric breakdown strength of alumina ceramics. *J. Eur. Ceram. Soc.* **2020**, *40*, 6218–6222. [CrossRef]
5. Wang, M.; Huang, X.; Du, J.; Chen, L.; Zhong, W. Synergistically improving dielectric breakdown strength and flashover voltage of a microstructure engineered alumina ceramic. *J. Alloys Compd.* **2025**, *1042*, 183947. [CrossRef]

6. Behera, R.P.; Ng, A.Y.R.; Du, Z.; Gan, C.L.; Le Ferrand, H. Ultrafast high temperature sintering and bioinspired microstructures as a more sustainable route to strong and tough alumina ceramics: A comparison with conventional sintering and challenges for high-performance. *J. Eur. Ceram. Soc.* **2026**, *46*, 118328. [CrossRef]
7. Fan, L.; Song, B.; Zhao, P.; Xia, X.; Tian, X.; Guo, X.; Guan, L.; Yang, S.; Zhang, M.; Sun, D.; et al. Fabrication of high-performance pure alumina ceramics with defect-rich structures by dynamic sinter forging. *Ceram. Int.* **2024**, *50*, 23188–23195. [CrossRef]
8. Han, Y.; Li, S.; Zhu, T.; Wu, W.; An, D.; Xie, Z. Enhanced properties of pure alumina ceramics by oscillatory pressure sintering. *Ceram. Int.* **2018**, *44*, 5238–5241. [CrossRef]
9. Xu, H.; Liu, R.; Bao, C.; Zhao, Y.; Cao, Z.; Huang, N.; Li, H.; Men, W.; Wu, X.; Zhang, S. The improvement of thermal shock resistance in alumina ceramics via vat photopolymerization by in-situ formation of mullite. *Ceram. Int.* **2025**, *51*, 46093–46106. [CrossRef]
10. Wahsh, M.M.S.; Khattab, R.M.; Awaad, M. Thermo-mechanical properties of mullite/zirconia reinforced alumina ceramic composites. *Mater. Des.* **2012**, *41*, 31–36. [CrossRef]
11. Dong, X.; Zheng, Y.; Xie, D.; Li, D. Multi-functional mullite fiber-based porous ceramics with a multilevel pore structure assembled by alumina platelets and mullite whiskers. *Ceram. Int.* **2023**, *49*, 847–854. [CrossRef]
12. Ren, B.; Kang, S.; Liu, J.; Wang, E.; Hou, X. Low-temperature preparation of alumina-mullite porous ceramic via gelation-assisted dual-phasic nanoparticle stabilized foams. *Ceram. Int.* **2024**, *50*, 29428–29436. [CrossRef]
13. Kool, A.; Thakur, P.; Bagchi, B.; Hoque, N.A.; Das, S. Mechanical, dielectric and photoluminescence properties of alumina–mullite composite derived from natural Ganges clay. *Appl. Clay Sci.* **2015**, *114*, 349–358. [CrossRef]
14. Feng, Q.; Yao, M.; Su, Z.; Yao, X. Significantly enhanced energy density of amorphous alumina thin films via silicon and magnesium co-doping. *Ceram. Int.* **2018**, *44*, 11160–11165. [CrossRef]
15. Ren, L.; Zeng, X.; Zhang, X.; Sun, R.; Tian, X.; Zeng, Y.; Xu, J.-B.; Wong, C.-P. Silver nanoparticle-modified alumina microsphere hybrid composites for enhanced energy density and thermal conductivity. *Compos. Part A Appl. Sci. Manuf.* **2019**, *119*, 299–309. [CrossRef]
16. Wu, X.; Song, G.; Zhang, X.; Lin, X.; Ivry, Y.; Tan, D.Q. Multilayer polyetherimide films incorporating alumina nanolayers for dielectric capacitors. *Chem. Eng. J.* **2022**, *450*, 137940. [CrossRef]
17. Tang, L.; Pan, Z.; Zhao, J.; Shen, Y.; Chen, X.; Li, H.; Li, P.; Zhang, Y.; Liu, J. Significantly enhanced energy storage capability of BNT-based ceramics via optimized sintering aids. *J. Alloys Compd.* **2023**, *935*, 168124. [CrossRef]
18. Mozalev, A.; Sakairi, M.; Takahashi, H.; Habazaki, H.; Hubálek, J. Nanostructured anodic-alumina-based dielectrics for high-frequency integral capacitors. *Thin Solid Films* **2014**, *550*, 486–494. [CrossRef]
19. Liu, H.; Yao, M.; Gao, W.; Su, Z.; Yao, X. Dual interfacial modification via anodizing method for achieving enhanced breakdown strength in multi-layer anodized alumina/$Sr_{0.85}Bi_{0.1}TiO_3$ films. *J. Alloys Compd.* **2020**, *817*, 152783. [CrossRef]
20. Bella, M.L.; Hamidouche, M.; Gremillard, L. Preparation of mullite-alumina composite by reaction sintering between Algerian kaolin and amorphous aluminum hydroxide. *Ceram. Int.* **2021**, *47*, 16208–16220. [CrossRef]
21. Zhang, C.; Zhang, Z.; Tan, Y.; Zhong, M. The effect of citric acid on the kaolin activation and mullite formation. *Ceram. Int.* **2017**, *43*, 1466–1471. [CrossRef]
22. Lin, S.-M.; Yu, Y.-L.; Zhong, M.-F.; Yang, H.; Liu, Y.; Li, H.; Zhang, C.-Y.; Zhang, Z.-J. Preparation of anorthite/mullite in situ and phase transformation in porcelain. *Materials* **2023**, *16*, 1616. [CrossRef]
23. Zhang, C.; Lu, S.; Zhang, Z.; Zhong, M.; Li, Y.; Huang, X.; Xu, W.; Wang, D.; Wang, L. The effect of phosphorus on the formation of mullite whiskers from citric acid activated kaolin. *Ceram. Int.* **2018**, *44*, 18796–18802. [CrossRef]
24. *ISO 13383-1:2012*; Fine Ceramics (Advanced Ceramics, Advanced Technical Ceramics)—Microstructural Characterization—Part 1: Determination of Grain Size and Size Distribution. ISO: Geneva, Switzerland, 2012.

Disclaimer/Publisher's Note: The statements, opinions and data contained in all publications are solely those of the individual author(s) and contributor(s) and not of MDPI and/or the editor(s). MDPI and/or the editor(s) disclaim responsibility for any injury to people or property resulting from any ideas, methods, instructions or products referred to in the content.